Electrospun Fe2O3-carbon composite nanofibers as durable anode materials for lithium ion batteries

Zhang, Xiang; Liu, Huihui; Petnikota, Shaikshavali; Ramakrishna, Seeram; Fan, Hong Jin

2014

Xiang, Z., Liu, H., Petnikota, S., Ramakrishna, S., & Fan, H. J. (2014). Electrospun Fe2O3-carbon composite nanofibers as durable anode materials for lithium ion batteries. Journal of materials chemistry A.

https://hdl.handle.net/10356/102104

https://doi.org/10.1039/c3ta15123a

Journal of Materials Chemistry A

Accepted Manuscript

This article can be cited before page numbers have been issued, to do this please use: Z. Xiang, H. Liu, S. Petnikota, S. Ramakrishna and H. J. Fan, *J. Mater. Chem. A*, 2014, DOI: 10.1039/C3TA15123A.

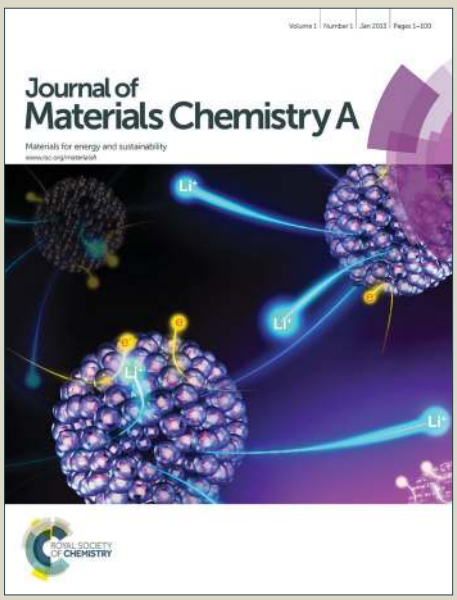

ROYAL SOCIETY OF CHEMISTRY

www.rsc.org/materialsA

Electrospun Fe_2O_3-carbon Composite Nanofibers as Durable Anode Materials for Lithium Ion Batteries

Xiang Zhang,[1,2] Huihui Liu,[3] Shaikshavali Petnikota,[4] Seeram Ramakrishna,[2] Hong Jin Fan[1*]

[1]Division of Physics and Applied Physics, School of Physical and Mathematical Sciences, Nanyang Technological University, Singapore 637371

[2] Center of Nanofibers & Nanotechnology, Department of Mechanical Engineering, Faculty of Engineering, National University of Singapore, 10 Kent Ridge Crescent, Singapore 117576

[3]Department of Medicine, Yong Loo Lin School of Medicine, National University of Singapore, 10 Kent Ridge Crescent, Singapore 119260

[4]School of Engineering Sciences and Technology (SEST), University of Hyderabad, Gachibowli, Hyderabad 500046, Andhra Pradesh, India

Abstract

Combination of metal oxides and carbon has been a favourable practice for their application in high-rate energy storage mesoscopic electrodes. We report quasi 1D Fe_2O_3–carbon composite nanofibers obtained by the electrospinning method, and evaluate them as the anode for Li ion storage. In the half-cell configuration, the anode exhibits a reversible capacity of 820 mA h g^{-1} at a current rate of 0.2C up to 100 cycles. At a higher current density of 5C, the cells still exhibit a specific capacity of 262 mAh g^{-1}. Compared to pure electrospun Fe_2O_3 nanofibers, the capacity retention of Fe_2O_3–C composite nanofiber electrode is drastically improved. The good electrochemical performance is associated with the homogenous dispersed Fe_2O_3 nanocrystals on the carbon nanofiber support. Such structure prevents the aggregation of active materials, maintains the structure integrity and thus enhances the electronic conductivity during lithium insertion and extraction.

Keywords: *Electrospinning, Lithium ion battery, Iron oxide, Carbon nanofibers, Energy storage*

View Article Online
DOI: 10.1039/C3TA15123A

Introduction

Lithium-ion batteries (LIBs), the commercialized rechargeable batteries, have been under the research focus in the past decade due to their extensive applications in portable electronics, electric vehicles (EVs) and hybrid electric vehicles (HEVs).[1] Commercial LIBs are made of $LiCoO_2$ positive electrode and graphite/carbon negative electrode. Graphite can form LiC_6 compound during lithiation and has a Li-storage capability of 372 A h kg^{-1}, which poses a storage limitation for high-energy applications. Besides the capacity limitation, graphite anode also faces severe safety problems of lithium plating during high current operation. Thus there is an increasing demand for the development of new anode materials with high specific capacity and power density from durable, nontoxic and inexpensive materials.

Transition metal oxides (e.g., MnO_2, Fe_2O_3, Fe_3O_4, Co_3O_4, etc) have been studied as a candidate for the anode materials, in view of their large theoretical capacity.[2-6] The lithium storage mechanism here is the 'conversion reaction' in which the transition metal oxides react with lithium ions leading to reversible *in situ* formation and decomposition of Li_yX (where X is O, S, F, or N).[2, 7] High reversible capacities ranging from 400 to 1100 mA h g^{-1} between 3.0 V and 0.001 V vs. Li/Li^+ can be generated from the reaction. Among the intensively studied transition metal oxides, Fe_2O_3 is an appealing anode material owing to its high theoretical capacity, high density (5.24 g cm^{-3} vs. 2.23 g cm^{-3} for graphite), low cost, earth abundance, environmentally friendly and high resistance to corrosion.[8-10] Fe_2O_3 can accommodate up to 6 moles of Li uptake/extraction per formula unit due to its high coordination number, leading to its high capacity of 1007 mA h g^{-1}. On the other hand, iron oxide anode materials are limited by a large capacity fading during cycling because of large volume change[11] and unavoidable thick solid electrolyte interphase (SEI) film on the Fe_2O_3 surface,[12-15] which results in pulverization, loss of electrical connection at high current rates and large irreversible capacity (consumption of large amount of Li^+ by SEI film). Furthermore, there is a significant hysteresis between Fe_2O_3 charge and discharge potentials around above 1 V. To overcome these problems, several strategies have been employed including carbon addition and nanoarchitecture control. Bruce and co-workers[16] compared the Li-cycling of nanosize, mesoporous, mm-size α-Fe_2O_3 particles and concluded that nanosize particles with a sufficient amount of added carbon (30 wt%) are essential to ensure high performance. Nanoparticles enhance the Li transport as well as ease the strain of the conversion reaction, and the added carbon improves the electronic transport to and within the nanoparticles.[16] Lou and co-workers[17] showed that addition of carbon, CNT and various coatings could enhance

View Article Online
DOI: 10.1039/C3TA15123A

the Li-storage performance of oxide materials; a very stable capacity of 800 mA h g^{-1} for 100 cycles at a current density of 500 mA g^{-1} can be obtained on the carbon coated Fe_2O_3 nanohorns on carbon nanotubes. Another issue with carbon-Fe_2O_3 is that the high temperature (≥600 ^oC) treatments can cause reduction of Fe_2O_3 to Fe.[14, 18] In short, while it is rather necessary for iron oxides to form composite with carbon, it still remains a challenge to fabricate nanostructured iron oxide and carbon in a form of uniform composites.

Compared to other synthesis methods such as forced hydrolysis, sol–gel synthesis, template methods, molten salt process, spray pyrolysis, hydrothermal method, co-precipitation technique,[19-26] electrospinning is a versatile, low cost and high-yield fabrication technique to pattern 1D nanofibers [27, 28] for various applications such as dye-sensitized solar cells[29, 30], photocatalysis[29], photodetector[31], supercapacitors[32, 33] and lithium ion batteries.[34-37] Here, we report the synthesis of Fe_2O_3–carbon hybrid ultralong nanofibers prepared by the well-established electrospinning technique. After calcination, Fe_2O_3 nanocrystals are formed and dispersed uniformly on the carbon fibers. The electrochemical properties of Fe_2O_3–C composite nanofibers are evaluated as the Li-ion battery anode, which indeed shows dramatically enhancement in cyclic stability compared to pure Fe_2O_3 particle fibers without carbon matrix.

Experimental

Synthesis of Fe_2O_3–C composite nanofibers

Polyacrylonitrile (PAN, Mw = 150,000), iron (III) acetylacetonate ($Fe(AcAc)_3$, > 99.9%), N,N-dimethylformamide (DMF, 99.8%) were purchased from Sigma-Aldrich and used as received.

In a typical process, 0.8 g of PAN was added into 20 mL DMF and stirred at 60 ^oC for 8 h. After that, 2.4 g of $Fe(AcAc)_3$ was slowly added into the above solution and stirred continuously for 8 h to yield homogeneous solution. The prepared homogeneous solution was then loaded into plastic syringes (10 mL) with a needle of 22G and subsequently placed into a commercial electrospinning setup (Electrospunra, Microtools Pte.Ltd Singapore). A high-voltage power of 20 kV was applied to the needle tip. The flow rate of fluid was set to 1 mL/h. The humidity level inside the electrospinning chamber was 55 ± 5%. The nanofibers were collected on aluminum foil wrapped around a flat plate placed 12 cm below the needle tip. The as-electrospun $Fe(AcAc)_3$-PAN composite nanofibers were first stabilized at 280 °C

for 3 h in Air. The as-stabilized sample was carbonized at 500 ^{o}C for 3h in Ar. The heating and cooling rate was set to be 2.5 °C/min.

Pure Fe_2O_3 nanofibers were also synthesized by electrospinning for comparison. The precursor solution consisting of $Fe(AcAc)_3$, polyvinyl pyrrolidone (PVP, MW= 100 000, Aldrich), and ethanol was loaded into a plastic syringe and a 20 kV DC voltage was applied to the single nozzle spinneret. The flow rate was set to 1 mL/h. The collector was grounded and placed at a distance of 12 cm below the spinneret. The as-spun samples were calcined at 500 ^{o}C for 3h in Air with a heating and cooling rate of 2.5 °C/min.

Characterization

Powder X-ray diffraction measurement was carried out using Bruker AXS D8 Advance X-ray diffractometer equipped with Cu Kα radiation between 20° and 80°. The morphological features and chemical composition were examined with a field emission scanning electron microscope (FE-SEM, JEOL-6701F). Particle morphology of the synthesized composites was observed using transmission electron microscopy (TEM, JEOL 3010) with an energy dispersive X-ray spectrometer (EDS) attachment and selected area electron diffraction (SAED). Specimens were prepared by ultrasonically dispersing Fe_2O_3–C composite nanofibers in ethanol followed by dropping the suspension on a carbon-coated copper grid. Raman spectrum was recorded by a Dilor model OMARS 89-Z24 microprobe spectrometer, under excitation of an Ar^+ ion laser of 514.5 nm. The surface area was determined by nitrogen adsorption/desorption using the Brunaue−Emmett−Teller method (BET, Micromeretics Tristar 2000). The sample was degassed under nitrogen gas at 300 °C for 10 h prior to BET measurements (under standard protocols at 77 K). The details of degas process and measurements are given in our previous study.[29, 36]

Electrochemical Measurements

All the electrochemical studies were conducted in two-electrode coin cell (CR 2016) configuration. The composite anode was prepared by mixing of active material (Fe_2O_3–C composite nanofibers), conductive additive (super P) and binder (Polyvinylidene fluoride, PVDF) in the mass ratio 70:15:15. This mixture was coated on an etched Cu foil (thickness 10 μm), which serves as current collector, and subsequently dried at 85 °C overnight before conducting cell assembly in an Ar-filled glovebox (MMM Ensaca). The circular electrode area and weight were 2 cm^2 and ~2.5 mg. The coin cells were assembled by lithium metal foil (Kyokuto Metal Co., Japan) as counter electrode, glass microporous fiber filter (Whatman,

Cat. No. 1825-047) as separator and 1 M $LiPF_6$ in ethylene carbonate (EC)/diethyl carbonate (DEC) (1:1 by volume, DAN VEC) as the electrolyte. Cyclic voltammetric (CV) traces were performed using Arbin automatic battery cycler at scan rate of 0.05 mV s^{-1} between 0.005 and 3.0 V. The galvanostatic discharge-charge cycling of the cells were carried out at different current densities between potentials of 0.005 and 3.0V by Arbin automatic battery cycler. Electrochemical impedance spectroscopy (EIS) (Solartran 1260+1287) technique was used to measure impedance in the frequency range from 0.003 Hz–180 KHz with an AC amplitude of 10 mV.

Results and discussions

The surface morphology of Fe_2O_3–C composite nanofibers was characterized using FESEM. The as-spun $Fe(AcAc)_3$–PAN composite nanofibers are randomly oriented, continuous with smooth surfaces as shown in Fig 1 (a). The $Fe(AcAc)_3$ counterpart in the composite nanofibers is amorphous. The diameter of the as-spun $Fe(AcAc)_3$–PAN composite nanofibers is in the range of 450–1200 nm. The inset is the optical image of as-spun $Fe(AcAc)_3$-PAN composite nanofibers deposited on aluminum foil. It can be peeled off readily from the aluminum foil as a free-standing nanofiber mat. Fig. 1 (b) shows the stabilized composite nanofibers mat after heating at 280 ^oC in air. During the stabilization process, the PAN counterpart was converted to an aromatic cyclized ladder type structure by cyclization, dehydrogenation, aromatization and crosslinking, which convert the CH_2 and C≡N groups to infusible C=N and C−H groups.[38] The as-stabilized composite nanofibers mat was further transformed to Fe_2O_3–C composite nanofibers after a further calcination process. During this process, N was removed in the form of N_2, and the chains joined into graphitic planes. The morphology of Fe_2O_3–C composite nanofibers mat is shown in Fig 1 (c) and more detailed images in Fig. 1 (d)–(f). The average diameter of Fe_2O_3–C composite nanofibers became smaller, in the range of 220–600 nm, as a result of weight loss from the removal of various components during carbonization. Also, the surface of Fe_2O_3–C composite nanofibers became rough (Fig 1 (f)) because of the presence of Fe_2O_3 nanoparticles crystalized on the nanofiber surface.

The microstructure of Fe_2O_3–C composite nanofibers was further examined by TEM. Figure 2 (a) shows the typical microstructure of a single Fe_2O_3–C composite nanofiber. The Fe_2O_3 nanoparticles are uniformly distributed along the nanofibers. A close-up view of the

View Article Online
DOI: 10.1039/C3TA15123A

composite fiber in Fig 2 (b) reveals that most of the Fe_2O_3 nanocrystals are embedded within the carbon fibers, and some remain on the surface. The Fe_2O_3 crystals have a size range of 18 ± 8 nm, measured from the imaging software attached to TEM. The corresponding diffraction rings of (104), (110), (113), (024) and (116) in the selected area electron diffraction (SAED) patterns (Figure 2 (c)) confirm the formation of polycrystalline α–Fe_2O_3 in composite nanofiber. As shown in Figure 2 (d), the high-resolution TEM image reveals the lattice fringes from the α–Fe_2O_3 nanoparticles with an interplanar spacing of 0.37 nm, corresponding to the (012) plane of hematite phase. The energy dispersive X-ray spectrometry (EDS) mapping analysis of Fe_2O_3–C composite nanofibers is illustrated in Fig 2 (e)-(h). The EDS analysis revealed the molar ratio of Fe and O to be about 2:3 for the composite nanofibers, which is in good agreement with the stoichiometric ratio of Fe_2O_3. The corresponding EDS mapping images for the elements of C, O and Fe illustrate clearly a homogeneous distribution of Fe_2O_3 crystals and carbon through the composite nanofibers.

More crystal structural and phase characterizations were conducted using XRD and Raman. The XRD pattern of Fe_2O_3–C composite nanofibers is shown in Fig 3 (a). The diffraction peaks match well with the rhombohedral phase of hematite Fe_2O_3 (JCPDS 33-0664). In addition, the diffraction peaks observed at $2\theta = 31.7^o$, 45.6^o and 55.6^o indicates the presence of maghemite Fe_2O_3 with spinel structure. The amount of γ–Fe_2O_3 was calculated to be 11 %. The intensity of the XRD peaks are strong, indicating a highly crystallinity. The lattice parameters of α-Fe_2O_3 were evaluated from Rietveld refinement using TOPAS 3 software to be a = 5.034 Å and c = 13.74 Å. The average crystallite size was calculated using Scherrer formulas to be 22.9 nm, quite close to the TEM analysis result. The specific surface area of Fe_2O_3–C composite nanofibers was estimated to be 46 $m^2\ g^{-1}$, according to the N_2 adsorption and desorption isotherm (data shown in Supporting Information, Fig S5). The Raman spectrum of the Fe_2O_3–C composite nanofibers between 800 and 2000 cm^{-1} is shown in Fig 3 (b). The broadened characteristic frequencies at ~1350 and ~1580 cm^{-1} correspond to the D band and G bands of carbon matrix, respectively. The D-band (disorder-induced phonon mode) can be attributed to defects and disordered portions of carbon (sp^3-coordinated), whereas the G-band (graphite band) is indicative of ordered graphitic crystallites of carbon (sp^2-coordinated).[39] The intensity ratio of D and G bands (I_D/I_G) provides useful information about the amount of carbon defects: a higher intensity ratio means a higher concentration of defects in the graphite comprising sp^2 hybridization. The intensity ratio I_D/I_G of our Fe_2O_3–C composite nanofibers is found to be 1.09, indicating a

View Article Online
DOI: 10.1039/C3TA15123A

relative high amount of disordered sections and defects.

We now present the results of electrochemical properties. Cyclic voltammetry (CV) was first carried out to investigate the electrochemical reaction process of the electrode made from Fe_2O_3–C composite nanofibers. Fig. 4 (a) shows the first five cycles of CV trace of the composite nanofibers electrode at room temperature between 0.005 and 3.0 V. In the first cathodic sweep, the well-defined current peak was observed at 0.67 V vs. Li^+/Li, which is ascribed to the complete reduction of Fe (III) to Fe (0), the formation of Li_2O and the irreversible reductive reaction of electrolyte to form solid electrolyte interphase (SEI) film.[20, 40, 41] In the first anodic scan, two board overlapping current peaks at 1.62 V and 1.85 V corresponds to reversible oxidation of Fe (0) to Fe (II) and Fe (II) to Fe (III). For the second cycles, one cathodic peak appears at 0.98 V with decreased intensity, while two anodic peaks remain unchanged, indicating the irreversible phase transformation with the formation of SEI film in the first cycle and good reversible reaction of Fe (0) to Fe (II) and Fe (II) to Fe (III) respectively.[42] It is noteworthy that the current of the anodic and cathodic peaks remain nearly the same for subsequent cycles, suggesting good reversibility and structure stability during Li^+ intercalation and extraction processes. The pure Fe_2O_3 nanofibers electrode also exhibits a similar kind of redox reaction (see Fig. 4b), except for the difference in the peak intensity and a shift in the reduction peak from 0.83 V to 0.69 V from 2nd cycle to 5th cycle. Compared to the CV trace of Fe_2O_3–C composite nanofibers, the large deviation in the current peaks of Fe_2O_3 nanofibers electrode suggest a larger capacity fading during cycling.

Galvanostatic cycling profiles of Li/Fe_2O_3–C composite nanofiber half-cells were performed to provide the electrochemical performance of reversibility and cyclibility. The typical signature of the charge−discharge curves for first two cycles of Li/ Fe_2O_3–C cells are given in Figure 5 (a). The first discharge curve can be divided into three regions labeled as I, II, III. First, the cell was discharged from open circuit voltage (OCV) 2.8 V to intercalate lithium ions into the Fe_2O_3 matrix (eqn (1)).[22] In region I, a plateau can be observed at 1.1 V with a wide slop, which is attributed to the phase transformation from hexagonal $Li_xFe_2O_3$ to cubic $Li_2Fe_2O_3$ (eqn (2)).[3, 22] In region II, a distinct plateau can be observed at 0.85 V due to the complete reduction of Fe (III) to Fe (0) (eqn (3)).[3, 22] The Fe nanocrystals were dispersed into Li_2O matrix. In the region III, the electrolyte was reduced below 0.8 V and the SEI film was formed, which led to further lithium storage via an interfacial reduction at the metal-Li_2O boundary. Thus, the initial specific capacity of 1214 mAh g^{-1} exceeds the theoretical capacity of 1007 mAh g^{-1} (6 mol of Li per 1 mol of α-Fe_2O_3), corresponds to an uptake of 7.2 mol Li

View Article Online
DOI: 10.1039/C3TA15123A

per 1 mol of α-Fe_2O_3–C composite.

$$Fe_2O_3 + xLi^+ + xe^- \rightarrow Li_xFe_2O_3 \quad (1)$$

$$Li_xFe_2O_3 + (2\text{-}x)\ Li^+ + (2\text{-}x)\ e^- \rightarrow Li_2Fe_2O_3\ (cubic) \quad (2)$$

$$Li_2Fe_2O_3\ (cubic) + 4\ Li^+ + 4\ e^- \rightarrow 2Fe + 3Li_2O \quad (3)$$

When the cell was charged to 3 V, a smooth voltage profile was observed at 1.5 V, followed by a sloping plateau at 2.5 V and a steep up to 3 V. The first charge capacity was 875 mA h g^{-1}, corresponding to an irreversible capacity loss of 28%. During the second cycle, a sloping plateau in the range of 0.8–1.05 V appeared, and the specific capacity decreased to 856 mA h g^{-1}, indicating the irreversible nature of amorphous Li_2O matrix. The galvanostatic cycling profiles of subsequent cycles are nearly the same, indicating good stability during charge and discharge cycling.

The cycling performance of Li/Fe_2O_3–C composite nanofibers and Li/pure Fe_2O_3 nanofibers cell cycled between 0.005 and 3 V at 0.2 C was presented in Fig 5 (b). The pure Fe_2O_3 nanofibers were synthesized also by electrospinning. The composite nanofibers cell show a rather stable capacity throughout the cycling process. Furthermore, it is obvious that, after a few initial cycles, the Columbic efficiency was found to be over 96%. The cell displays a discharge capacity of 820 mA h g^{-1} even after 100 cycles, which corresponds to a 96% capacity retention. For comparison, the capacity of pure Fe_2O_3 nanofibers cells fades rapidly to 482 mA h g^{-1} after 100 cycles, corresponding to a 50 % capacity retention. The improved cycle stability and reversible specific capacity of Fe_2O_3–C composite nanofibers are attributed to uniform composite fiber structure in which Fe_2O_3 nanocrystals are well dispersed on the carbon matrix. This structure has the following advantages: The carbon matrix prevents the pulverization and aggregation of the Fe_2O_3 nanoparticles, accommodates the large volume change of Fe_2O_3 particles during cycling. The carbon improves the electronic conductivity and electrical contact with the active materials (see below). The one dimensional characteristics of the nanocomposite also provides a good mechanical integrity of the electrode.

Rate capability measurement was carried out on the Fe_2O_3–C composite nanofiber cells at various current densities (Figure 5 (c)). The discharge capacities is 973 mA h g^{-1} when cycled at a small current density of 0.1 C for 15 cycles. When increasing the current density to 0.2C, 0.5C, 1C, 2C and 5C, the corresponding specific capacity values are 871, 770, 631, 455, and 262 mA h g^{-1}, respectively. Importantly, the reversible capacity of 982 mA h g^{-1}

View Article Online
DOI: 10.1039/C3TA15123A

was still retained when the current density returned to 0.1 C after 75 cycles. This high rate capability is related to the thickness of SEI film, the interfacial charge transfer and lithium ion diffusion in the nanocomposite materials. The presence of carbon component is beneficial for the high rate performance of the cell for prolonged cycling.

In order to validate the mechanism of the difference in electrochemical performance between Fe_2O_3–C composite nanofibers and pure Fe_2O_3 nanofibers, an electrochemical impedance spectroscopy (EIS) was conducted. The Nyquist plots are present in Figure 5 (d). The EIS spectra of pure Fe_2O_3 and composite nanofibers have a similar shape, which consists of a semicircle in the high frequency range and an inclined line in the low frequency range. The EIS data were fit by an equivalent circuit as shown in Fig 5 (e). R_e is the ohmic resistance, which represents the total resistance of the electrolyte, separator and electrical contact. The semicircle in high-frequency region is attributed to the lithium ion migration resistance through a SEI film (R_{sf}) and the charge-transfer resistance (R_{ct}). CPE_{sf} and CPE_{dl} is the constant phase element, which represents the charges accumulated on both side of the electrode/electrolyte interface when lithium ion across. The inclined line corresponds to the lithium diffusion kinetics in the solid-state called as Warburg impedance (Wz).[43] The fitting results were summarized in Table S1 (See supporting information). It can be observed that R_{sf} and R_{ct} of Fe_2O_3–C composite nanofibers was 67 and 159 Ω compared to pure Fe_2O_3 nanofibers (112 and 192 Ω). The SEI resistance and charge-transfer resistance are reduced by the introduction of carbon into the 1D composite nanofibers. As expected, the carbon component uniformly distributed in 1D nanofibers improves the stability of SEI film, the rate of charge-transfer and the Li^+ kinetics, which results in a higher rate capability and improved cycling performance.

Conclusion

A new type of Fe_2O_3–carbon composite 1D nanofiber mats have been prepared by a facile and scalable electrospinning route for the application as the LIB anode material. The Fe_2O_3 nanocrystals are uniformly distributed on the carbon fiber matrix. Such composite nanofiber electrodes demonstrate an improved cycling stability, good reversibility and rate capability compared to pure electrospun Fe_2O_3 naonfibers. The enhanced electrochemical performance is ascribed to the unique structure of fiber mat with a stable structural integrity and improved electrical conductivity rendered by the carbon fiber network. Given the simple fabrication and outstanding performance, the Fe_2O_3–C nanocomposite fiber mats could be a prospective

View Article Online
DOI: 10.1039/C3TA15123A

high-performance anode material for LIBs. In addition, there is no limitation for the electrospinning route to other composite fibers with various metal oxides such as Co_3O_4, MoO_3, MnO_2, NiO for durable and flexible battery electrodes.

Acknowledgement

This work is financial supported by Public Sector Research Funding (Grant number 1121202012), Agency for Science, Technology, and Research (A*STAR), and by the Merlion 2011 project. Dr. H. Liu thanks the postdoc fellowship from Yong Loo Lin School of Medicine, NUS and Cardiovascular Research Institute, NUHS. The authors also acknowledge the help from Prof Ting Yu in Nanyang Technological University with glove box.

Reference

1. A. Yoshino, *Angew. Chem. Int. Ed.*, 2012, **51**, 5798-5800.
2. P. Poizot, S. Laruelle, S. Grugeon, L. Dupont and J. M. Tarascon, *Nature*, 2000, **407**, 496.
3. D. Larcher, C. Masquelier, D. Bonnin, Y. Chabre, V. Masson, J. B. Leriche and J. M. Tarascon, *J. Electrochem. Soc.*, 2003, **150**, A133-A139.
4. J. Luo, X. Xia, Y. Luo, C. Guan, J. Liu, X. Qi, C. F. Ng, T. Yu, H. Zhang and H. J. Fan, *Adv. Energy Mater.*, 2013, **3**, 737-743.
5. Y. Luo, J. Luo, J. Jiang, W. Zhou, H. Yang, X. Qi, H. Zhang, H. J. Fan, D. Y. W. Yu, C. M. Li and T. Yu, *Energy Environ. Sci.*, 2012, **5**, 6559-6566.
6. J. Luo, J. Liu, Z. Zeng, C. F. Ng, L. Ma, H. Zhang, J. Lin, Z. Shen and H. J. Fan, *Nano Lett.*, 2013.
7. P. L. Taberna, S. Mitra, P. Poizot, P. Simon and J. M. Tarascon, *Nat. Mater.*, 2006, **5**, 567.
8. Z. Wang, L. Zhou and X. W. Lou, *Adv. Mater.*, 2012, **24**, 1903-1911.
9. F. Han, D. Li, W.-C. Li, C. Lei, Q. Sun and A.-H. Lu, *Adv. Funct. Mater.*, 2013, **23**, 1692-1700.
10. B. Koo, H. Xiong, M. D. Slater, V. B. Prakapenka, M. Balasubramanian, P. Podsiadlo, C. S. Johnson, T. Rajh and E. V. Shevchenko, *Nano Lett.*, 2012, **12**, 2429-2435.
11. W. Chen, S. Li, C. Chen and L. Yan, *Adv. Mater.*, 2011, **23**, 5679-5683.
12. R. Liu, J. Duay and S. B. Lee, *Chem. Commun.*, 2011, **47**, 1384-1404.
13. J. Duay, S. A. Sherrill, Z. Gui, E. Gillette and S. B. Lee, *ACS Nano*, 2013, **7**, 1200-1214.
14. S. Yuan, Z. Zhou and G. Li, *Crystengcomm*, 2011, **13**, 4709-4713.
15. J. Hu, H. Li, X. Huang and L. Chen, *Solid State Ionics*, 2006, **177**, 2791-2799.
16. F. Jiao, J. Bao and P. G. Bruce, *Electrochem. Solid-State Lett.*, 2007, **10**, A264-A266.
17. Z. Wang, D. Luan, S. Madhavi, Y. Hu and X. W. Lou, *Energy Environ. Sci.*, 2012, **5**, 5252-5256.
18. T. Yoon, C. Chae, Y.-K. Sun, X. Zhao, H. H. Kung and J. K. Lee, *J. Mater. Chem.*, 2011, **21**, 17325-17330.
19. J. Liu, Y. Li, H. Fan, Z. Zhu, J. Jiang, R. Ding, Y. Hu and X. Huang, *Chem. Mater.*, 2009, **22**, 212-217.
20. S.-L. Chou, J.-Z. Wang, D. Wexler, K. Konstantinov, C. Zhong, H.-K. Liu and S.-X. Dou, *J. Mater. Chem.*, 2010, **20**, 2092-2098.
21. M. F. Hassan, M. M. Rahman, Z. P. Guo, Z. X. Chen and H. K. Liu, *Electrochim. Acta*, 2010, **55**, 5006-5013.

22. D. Larcher, D. Bonnin, R. Cortes, I. Rivals, L. Personnaz and J.-M. Tarascon, *J. Electrochem. Soc.*, 2003, **150**, A1643-A1650.
23. X.-L. Wu, Y.-G. Guo, L.-J. Wan and C.-W. Hu, *J. Phys. Chem. C*, 2008, **112**, 16824-16829.
24. Y. NuLi, P. Zhang, Z. Guo and H. Liu, *J. Electrochem. Soc.*, 2008, **155**, A196-A200.
25. X. W. Lou, C. Yuan and L. A. Archer, *Small*, 2007, **3**, 261-265.
26. H. Liu, G.-K. Chuah and S. Jaenicke, *J. Catal.*, 2012, **292**, 130-137.
27. D. Li and Y. Xia, *Adv. Mater.*, 2004, **16**, 1151-1170.
28. B. Lu, Y. Wang, Y. Liu, H. Duan, J. Zhou, Z. Zhang, Y. Wang, X. Li, W. Wang, W. Lan and E. Xie, *Small*, 2010, **6**, 1612-1616.
29. X. Zhang, V. Thavasi, S. G. Mhaisalkar and S. Ramakrishna, *Nanoscale*, 2012, **4**, 1707-1716.
30. Y. Li, D.-K. Lee, J. Y. Kim, B. Kim, N.-G. Park, K. Kim, J.-H. Shin, I.-S. Choi and M. J. Ko, *Energy Environ. Sci.*, 2012, **5**, 8950-8957.
31. X. Li, C. Gao, H. Duan, B. Lu, Y. Wang, L. Chen, Z. Zhang, X. Pan and E. Xie, *Small*, 2013, **9**, 2005-2011.
32. C. Kim, J.-S. Kim, S.-J. Kim, W.-J. Lee and K.-S. Yang, *J. Electrochem. Soc.*, 2004, **151**, A769-A773.
33. Y.-E. Miao, W. Fan, D. Chen and T. Liu, *ACS Appl. Mater. Interfaces*, 2013, **5**, 4423-4428.
34. A. D. Su, X. Zhang, A. Rinaldi, S. T. Nguyen, H. Liu, Z. Lei, L. Lu and H. M. Duong, *Chem. Phys. Lett.*, 2013, **561–562**, 68-73.
35. X. Zhang, V. Aravindan, P. S. Kumar, H. Liu, J. Sundaramurthy, S. Ramakrishna and S. Madhavi, *Nanoscale*, 2013, **5**, 5973-5980.
36. X. Zhang, P. Suresh Kumar, V. Aravindan, H. H. Liu, J. Sundaramurthy, S. G. Mhaisalkar, H. M. Duong, S. Ramakrishna and S. Madhavi, *J. Phys. Chem. C*, 2012, **116**, 14780-14788.
37. J. Zhu, G. Zhang, X. Yu, Q. Li, B. Lu and Z. Xu, *Nano Energy*, 2014, **3**, 80-87.
38. S. Hamideh Mortazavi, S. Pilehvar, M. Ghoranneviss, M. T. Hosseinnejad, S. Zargham, A. Mirarefi and A. Mirarefi, *Appl. Phys. A*, 2013, **113**, 703-712.
39. A. C. Ferrari, J. C. Meyer, V. Scardaci, C. Casiraghi, M. Lazzeri, F. Mauri, S. Piscanec, D. Jiang, K. S. Novoselov, S. Roth and A. K. Geim, *Phys. Rev. Lett.*, 2006, **97**, 187401.
40. H. Liu, G. Wang, J. Wang and D. Wexler, *Electrochem. Commun.*, 2008, **10**, 1879-1882.
41. B. Wang, J. S. Chen, H. B. Wu, Z. Wang and X. W. Lou, *J. Am. Chem. Soc.*, 2011, **133**, 17146-17148.
42. Y. Song, S. Qin, Y. Zhang, W. Gao and J. Liu, *J. Phys. Chem. C*, 2010, **114**, 21158-21164.
43. A. J. Bard and L. R. Faulkner, *Electrochemical Methods: Fundamentals and Applications*, 2001.

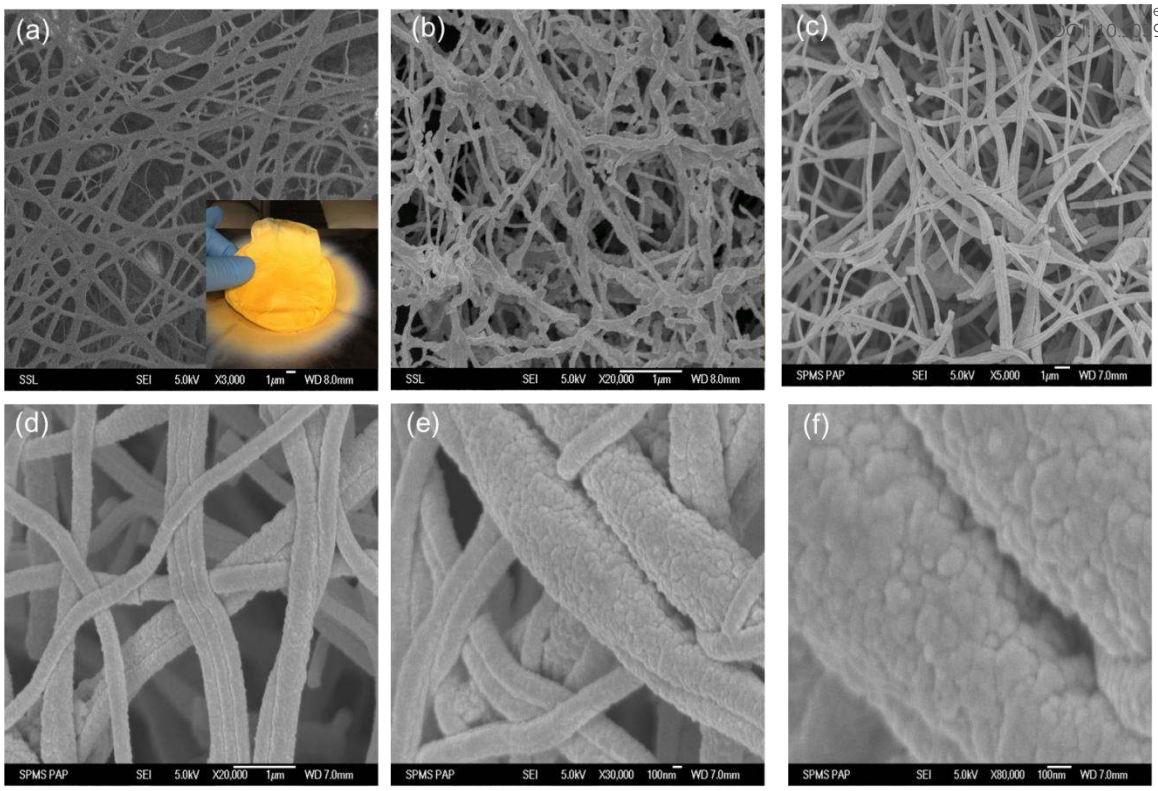

Fig 1 (a) FESEM image of the as-spun nanofiber mat; (b) The nanofiber mat after stabilization by annealing at 280°C in Air; (c) The Fe_2O_3–C composite nanofiber mat after carbonization at 500 °C in argon; (d)-(f) Close-up views of Fe_2O_3–C composite nanofibers after calcination at 500 °C in argon.

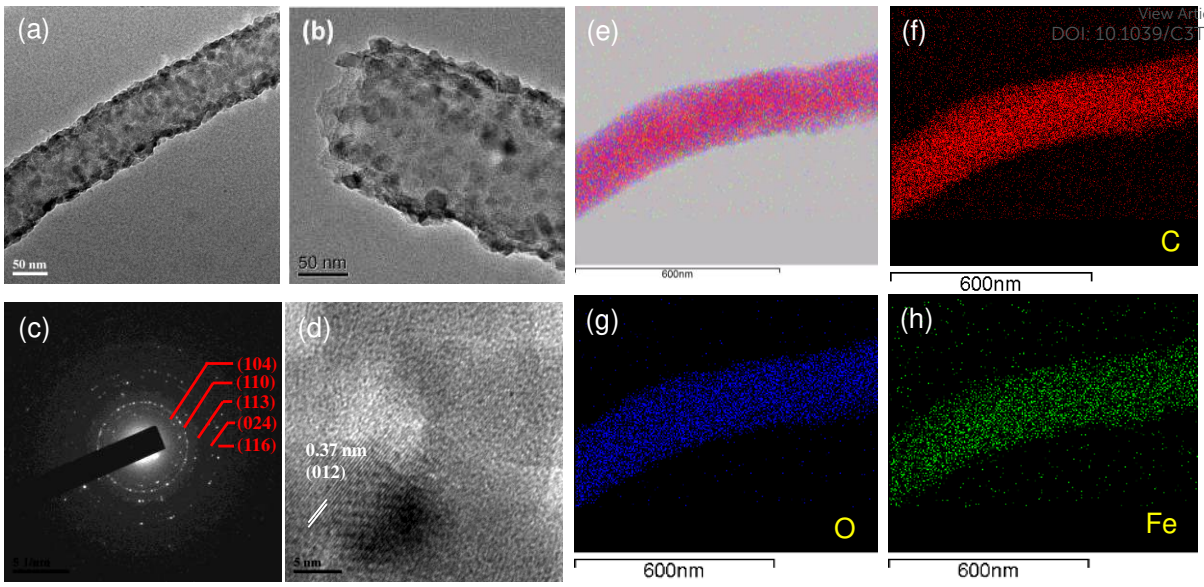

Fig 2. TEM characterization of the Fe_2O_3–C composite nanofibers. (a) Typical structure of the composite nanofiber; (b) The tip of one composite nanofiber; (c) The corresponding SAED pattern; (d) HRTEM image of the hematite Fe_2O_3 crystals; (e) TEM image of a single Fe_2O_3–C composite nanofiber with elements mapping; (f)-(h) Element mappings of carbon (red), oxygen (blue), and iron (green), respectively.

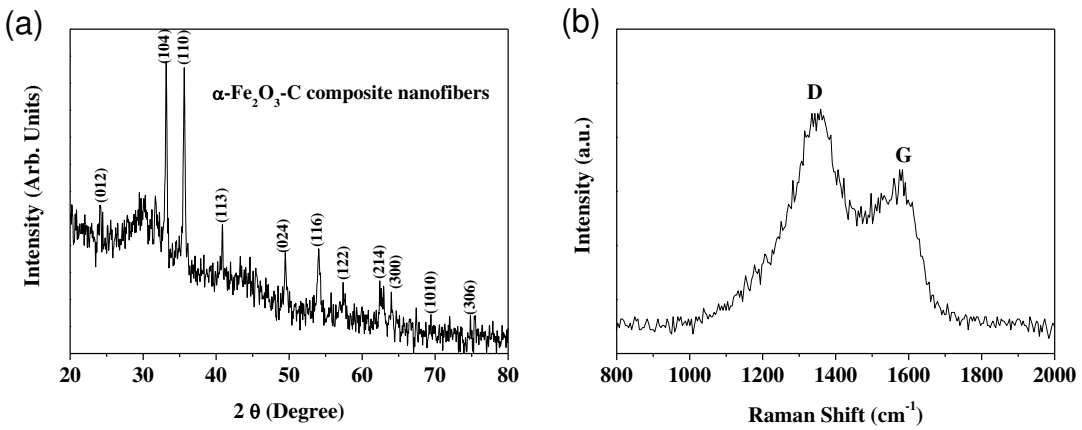

Fig 3 (a) X-ray diffraction patterns and (b) Raman spectrum of the Fe_2O_3–C composite nanofibers.

View Article Online
DOI: 10.1039/C3TA15123A

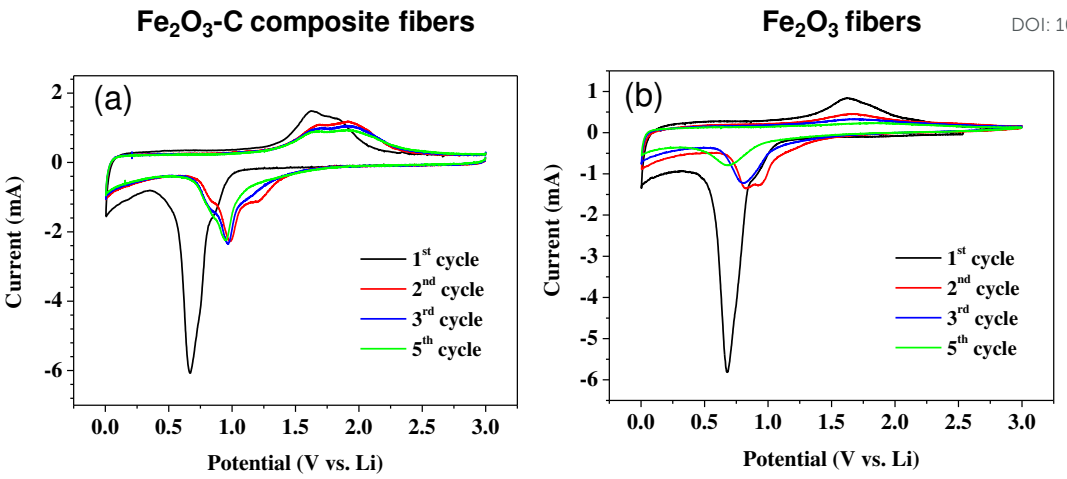

Fig 4 Cyclic voltammogram of (a) Fe_2O_3–C composite nanofiber and (b) pure Fe_2O_3 nanofiber half-cells cycled between 0.005 and 3 V at a scan rate of 0.05 mV s^{-1}, in which metallic lithium serves as both counter and reference electrode.

View Article Online
DOI: 10.1039/C3TA15123A

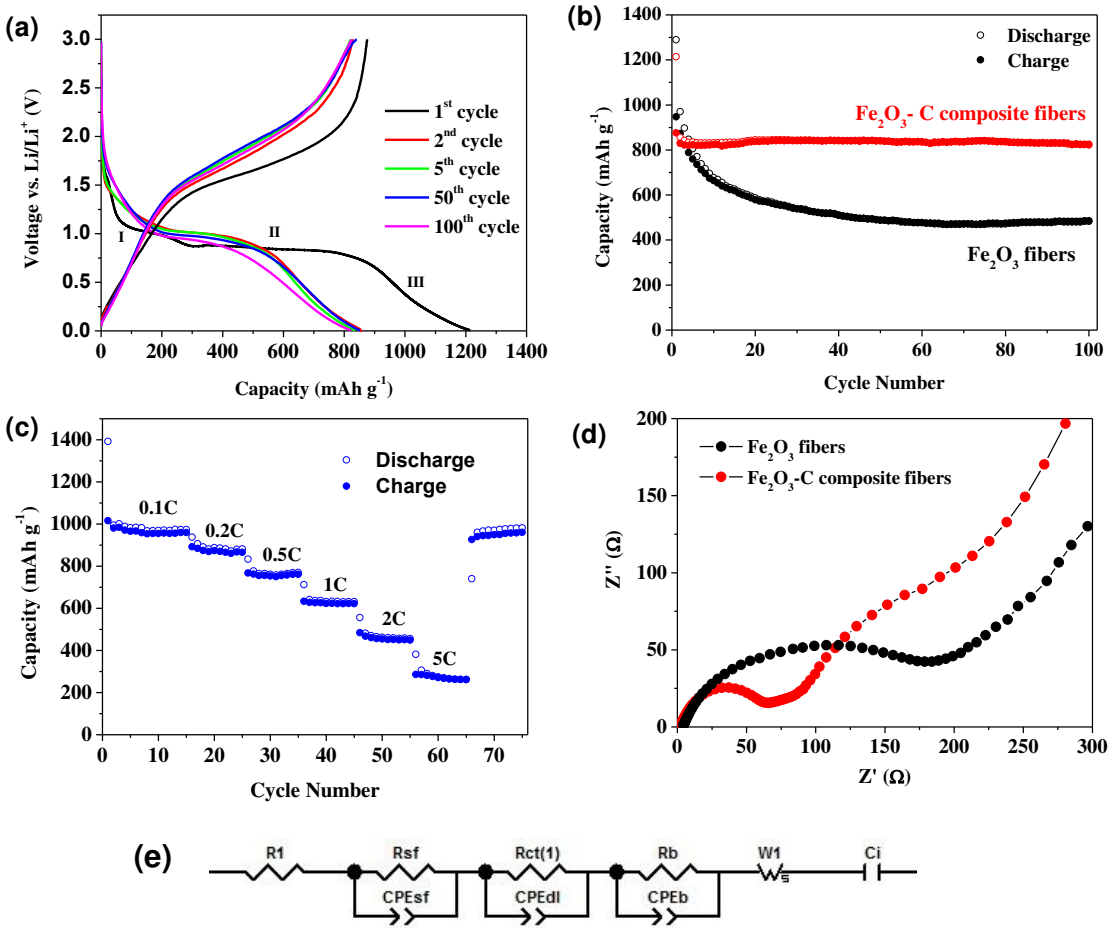

Fig 5 (a) Galvanostatic charge-discharge curves of Fe_2O_3–C composite nanofibers electrode cycled between 0.005 and 3 V (vs. Li/Li^+) at 0.2 C rate (1 C =1007 mA g^{-1}); (b) Cyclic performance of Fe_2O_3–C composite nanofiber and pure Fe_2O_3 nanofiber electrodes at 0.2 C rate; (c) Rate capability of Fe_2O_3–C composite nanofiber electrodes at different rates; (d) Nyquist plots of Fe_2O_3–C composite nanofiber and pure Fe_2O_3 nanofiber electrodes; (e) The equivalent circuit to fit the EIS spectra.

TOC Figures

View Article Online
DOI: 10.1039/C3TA15123A